ORNL/MDF-TC-2019-161
CRADA/NFE-19-07678

Additively Manufacturing Nitinol Shape Memory Alloys for Advanced Actuator Designs

Alex Plotkowski
Kyle Fezi
Chris Fancher
Peeyush Nandwana
Fred List
Keith Carver
Brian Jordan
Desarae Goldsby

July, 2023

OAK RIDGE NATIONAL LABORATORY
MANAGED BY UT-BATTELLE FOR THE US DEPARTMENT OF ENERGY

ORNL/MDF-TC-xxxxx
CRADA/NFE-19-07678

Materials Science and Technology Division
Advanced Manufacturing Office

Additive Manufacturing Nitinol Shape Memory Alloys for Advanced Actuator Designs

Alex Plotkowski
Kyle Fezi
Chris Fancher
Peeyush Nandwana
Fred List
Keith Carver
Brian Jordan
Desarae Goldsby

Date Published:
July 1, 2023

Prepared by
OAK RIDGE NATIONAL LABORATORY
Oak Ridge, Tennessee 37831-6283
managed by
UT-BATTELLE, LLC
for the
US DEPARTMENT OF ENERGY
under contract DE-AC05-00OR22725

CONTENTS

LIST OF FIGURES

ACKNOWLEDGEMENTS

This CRADA NFE-19-0767 was conducted as a Technical Collaboration project within the Oak Ridge National Laboratory (ORNL) Manufacturing Demonstration Facility (MDF) sponsored by the US Department of Energy Advanced Manufacturing Office (CPS Agreement Number 24761). Opportunities for MDF technical collaborations are listed in the announcement "Manufacturing Demonstration Facility Technology Collaborations for US Manufacturers in Advanced Manufacturing and Materials Technologies" posted at http://web.ornl.gov/sci/manufacturing/docs/FBO-ORNL-MDF-2013-2.pdf. The goal of technical collaborations is to engage industry partners to participate in short-term, collaborative projects within the Manufacturing Demonstration Facility (MDF) to assess applicability and of new energy efficient manufacturing technologies. Research sponsored by the U.S. Department of Energy, Office of Energy Efficiency and Renewable Energy, Advanced Manufacturing Office, under contract DE-AC05-00OR22725 with UT-Battelle, LLC.

ABSTRACT

The objective of this research was to understand the role of feedstock production in the phase transformation behavior of additively manufactured Ni-Ti alloys for advanced actuator design. Industrial adoption of additively manufactured Ni-Ti alloys depends on the ability to produce repeatable phase transformation behavior, quantified here by the austenite to martensite transformation on heating. Small variations in the alloy composition may have a significant effect on the temperature at which this transformation occurs. This project showed that the powder characteristics play an important role in determining this behavior. Increases in the surface area per unit volume of the powder, either as a function of size distribution or morphology, have the effect of reducing the Ti content in the alloy through the formation of Ti-rich oxides on the powder surface, which has the effect of depressing the transformation temperature. Preferential Ni vaporization during additive manufacturing can partially offset this effect. To achieve repeatable results, it is important to understand the effect of powder oxidation, and to control the powder characteristics.

1. ADDITIVE MANUFACTURING OF NITINOL SHAPE MEMORY ALLOYS

This phase 1 technical collaboration project (MDF-TC-2019-161) was begun on April 1, 2019 and was completed on May 30, 2023. The collaboration partner Fort Wayne Metals is a large business. The project found that powder size distribution and morphology plays a critical role in determining the austenite to martensite transformation temperature in additively manufactured Ni-Ti alloys. The powder surface area per unit volume dictates the amount of Ti-rich oxide that forms on the powder surface, which affects the transformation behavior by reducing Ti content in the alloy powder. This effect is somewhat counteracted by preferential Ni vaporization during additive processing, which in turn depends on process conditions. Importantly, this result indicates that careful control of powder size distribution and morphology is critical for achieving the desired phase transformation characteristics.

1.1 BACKGROUND

The Ni-Ti binary alloy system exhibits a solid-solid phase transformation from austenite to martensite which results in both shape memory and superelastic properties, in which the material may recover very large strain in response to either heat or unloading, respectively [1]. Since the discovery of this microstructural phenomenon in the 1960s [2], Ni-Ti alloys, known commercially as Nitinol, have been adopted for a variety of applications. Among these, Nitinol has been increasingly used in actuator design in the aerospace [3,4] and automotive [4–6] (Figure 1) industries. These actuators have been used to replace more complex electromechanical and hydraulic actuators, resulting in a reduction in system complexity, improved reliability, and weight savings. The solid-state austenite to martensite transformation in Ni-Ti also exhibits excellent elastocaloric [7] properties that makes it ideal for future applications in cooling and refrigeration.

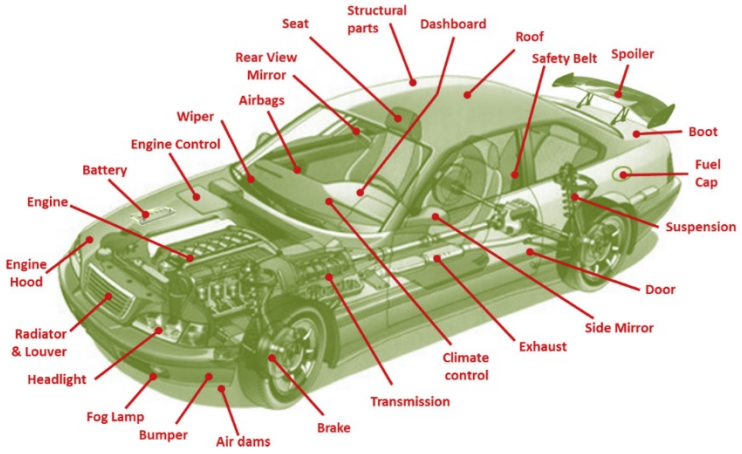

Figure 1: Diagram showing existing and potential automotive applications for shape memory alloys [4]**.**

Although most Nitinol products are manufactured via casting and subsequent deformation and thermal processing, recent research has shown increased potential for production of unique, complex geometries by additive manufacturing (AM) [8]. Conventional processing of Nitinol is limited to simple product forms such as tubes, bars and wires, and production of more complex shapes requires machining with large yield losses. Nitinol is also notoriously difficult and expensive to machine. Conventional processing therefore limits practical application of Nitinol to simple torsional or linear motion actuators. AM offers a route to developing next-generation actuators with more complex motion in advanced actuators, with a dramatic reduction in machining and increase in yield.

However, the major barrier to adoption of AM for production of Nitinol is the extreme sensitivity of the solid-state phase transformation behavior to chemistry, micro-cleanliness, and heat treatment. For example, the transformation temperature has been shown to be a strong function of both nominal composition and volumetric energy density in laser powder bed fusion processing [9].

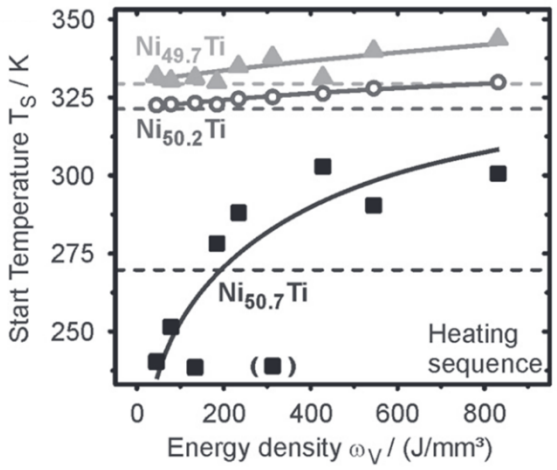

Figure 2: Example of variation in transformation temperature as a function of alloy chemistry and AM process conditions [9]**.**

The goal of this work is to understand the difference in material quality and transformation behavior for additively manufactured Nitinol as a function of the Ni-Ti composition as compared to conventionally processed products. For specific applications, the transformation temperature must be carefully

controlled, and the behavior of conventional materials produced by Fort Wayne Metals during the atomization process and subsequent additive processing is currently unknown.

1.2 TECHNICAL RESULTS

1.2.1 Phase 1

In Phase 1 of the project, three different Nitinol alloy compositions were evaluated for laser powder bed fusion (LPBF) additive manufacturing. There different powders were manufacturing and then used for LPBF processing. The powder and printed components were characterized and compared.

1.2.1.1 Initial powder characterization

Fort Wayne Metals (FWM) produced three ingots and commissioned them for gas atomization. The nominal compositions of the powder were measured as shown in Table 1. The powders were then sieved to isolate a size distribution suitable for powder bed additive manufacturing.

Table 1: Measured powder compositions.

Alloy Designation	Certified Ni Composition (wt. %)	Certified Ni Composition (at.%)
Alloy A	54.8	49.8
Alloy B	55.8	50.8
Alloy C	56.0	51.0

The resulting powder was characterized using scanning electron microscopy and a Malvern Morphologi G3 optical particle size distribution measurement system. Some representative micrographs of powder particles for each alloy are summarized in Figure 3. In all three cases, while most of the powder particles are smooth and roughly spherical, there is a second population of particles with rough surfaces and high aspect ratios. Alloy C appears to have the greatest number of these irregular particles. Due to their increased roughness, it is anticipated that this sub-population of particles will have an increased average surface area per unit volume. The powder size distribution used for each alloy was measured as shown in Figure 4, reported as weighted by both the number frequency, which emphasizes small particles, and by volume frequency, which emphasizes large particles. For Alloys B and C where the nominal size distribution was 53-109 μm, a wider size distribution was observed compared to Alloy A, where the nominal size range was 20-53 μm. The largest particles in the volume weighted distribution appear to roughly correspond to the nominal size ranges, indicating that the largest particles were effectively screened. However, the smallest particles, apparent in the number weighted distributions, were not sieved effectively. Alloy B has the widest distribution containing both the highest fraction of fine particles, but also a significant population of large particles.

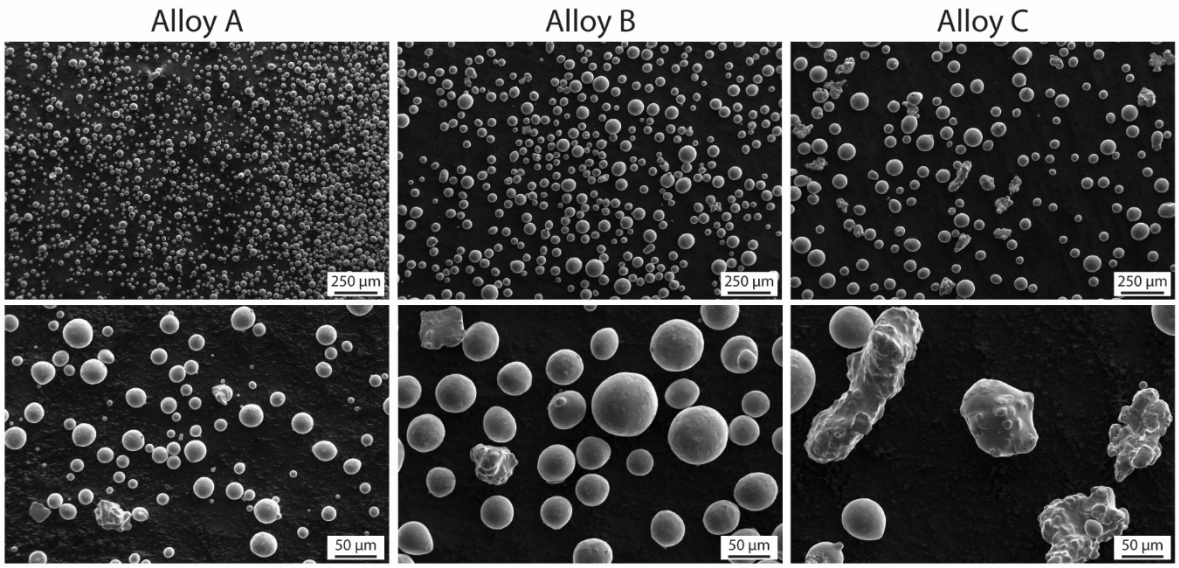

Figure 3: Representative powder SEM micrographs.

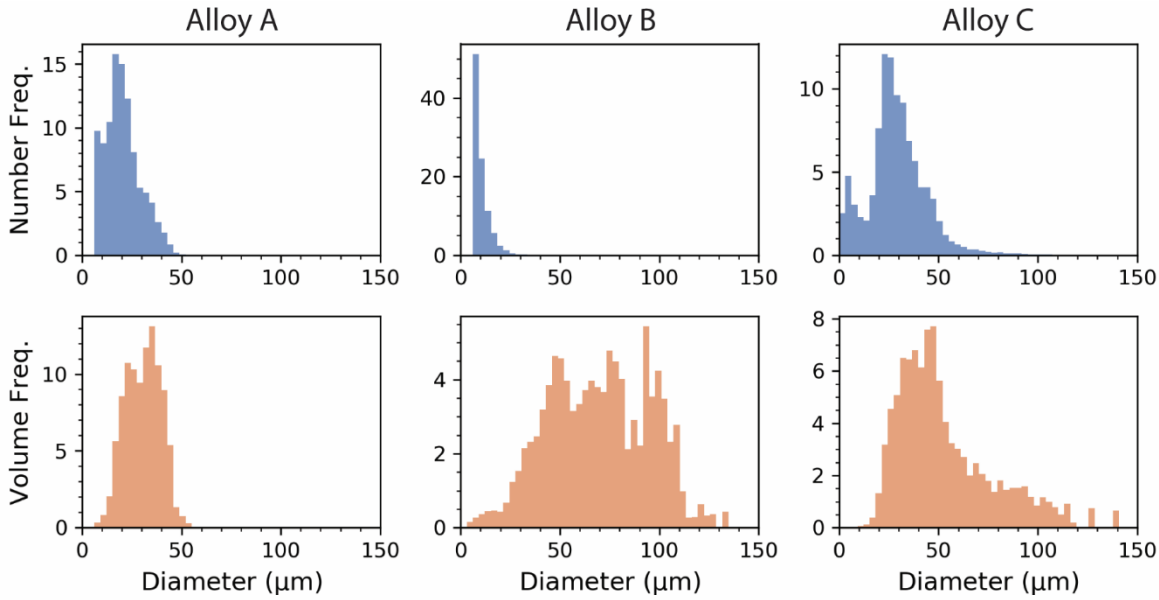

Figure 4: Histograms showing the measured powder size for each alloy.

Differential scanning calorimetry (DSC) was used to measure the phase transformation behavior of the as-atomized powders. Results on heating and cooling are compared for each alloy in Figure 5. Generally, the DSC curves for the finest powder is poorly defined, with several weak peaks that are often spread over a wide temperature range. With increasing powder size, the cooling rate of the powder during atomization tends to slow. The resulting peaks in the DSC curves become more well defined, although they also contain secondary peaks indicative of a non-equilibrium phase distribution.

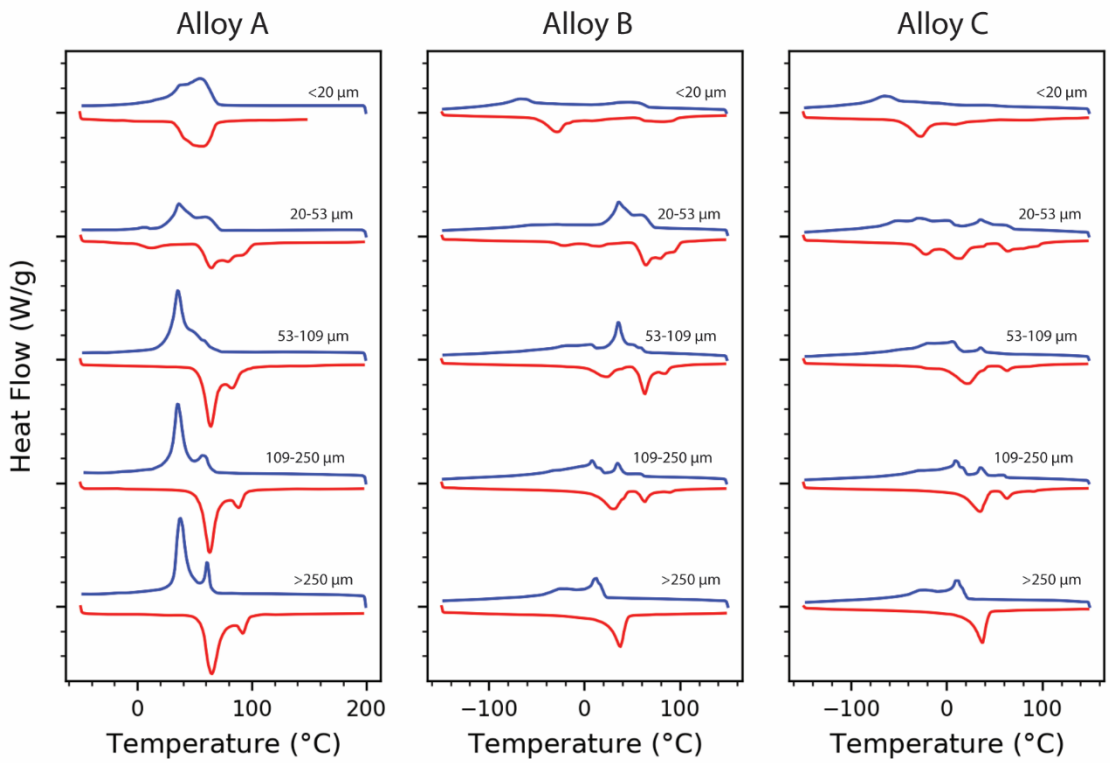

Figure 5: DSC results for powder as a function of size distribution for each alloy.

1.2.1.2 Laser Powder Bed Fusion Builds and Characterization

Additive manufacturing was performed using a Renishaw AM250 system. This AM system uses a pulsed laser such that the primary process variables are the laser power, pulse exposure time, the point-to-point spacing between pulses, hatch spacing, and the layer thickness. For each of the three alloys, a design of experiments was performed to evaluate the effect of process conditions on material densification (Table 2). However, for the purpose of this study, a single parameter set (the central point of the design of experiments) was used to compare the three alloys against each other. Considering that it is well known that changes in volumetric energy density can alter the solid-state phase transformation temperature by changing the level of preferential Ni vaporization [14], holding the process conditions constant between alloys isolates the influence of composition and powder characteristics. All builds were performed in an argon atmosphere, with atmospheric oxygen controlled below 500 ppm.

Alloy A was processed using the 20-53 µm nominal size distribution. Difficulties with flowability in this powder however motivated use of a larger size distribution (nominally 53-109 µm) for the other two alloys. Also, a Ti-6Al-4V baseplate was used for Alloy A, but due to delamination defects observed during this build, NiTi base plates were used for Alloys B and C. Photographs of the completed builds are shown in Figure 6. The selected samples from each were from a series of replicates of the central parameter set (cubes 15-25, see numbering for Alloy A).

Table 2: Process conditions for the design of experiments.

Run #	Power(W)	Layer Thickness (µm)	Hatch Space (µm)	Point Spacing (µm)	Exp Time (µs)	V_{eff} (m/s)	Duty Cycle (%)	Lin. Heat Input (J/m)	Vol. Heat Input (J/mm³)	Build Rate (cc/hr)
1	200	30	100	70	25	1.707	61.0	71	24	18.4
2	200	30	100	70	55	0.986	77.5	157	52	10.6
3	200	30	100	80	25	1.860	58.1	63	21	20.1
4	200	30	100	80	55	1.096	75.3	138	46	11.8
5	200	30	115	70	25	1.707	61.0	71	21	21.2
6	200	30	115	70	55	0.986	77.5	157	46	12.2
7	200	30	115	80	25	1.860	58.1	63	18	23.1
8	200	30	115	80	55	1.096	75.3	138	40	13.6
9	200	30	108	75	20	2.027	54.1	53	16	23.6
10	200	30	108	75	65	0.915	79.3	173	53	10.7
11	200	30	108	67	40	1.209	72.2	119	37	14.1
12	200	30	108	83	40	1.416	68.3	96	30	16.5
13	200	30	95	75	40	1.316	70.2	107	37	13.5
14	200	30	120	75	40	1.316	70.2	107	30	17.1
15-25	200	30	108	75	40	1.316	70.2	107	33	15.3

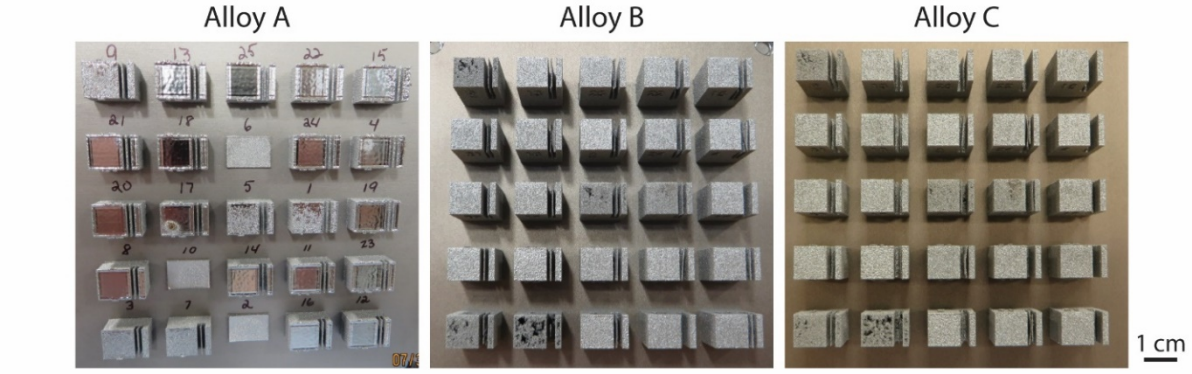

Figure 6: Photographs of design of experiment builds for each alloy.

Samples from the LPBF builds of each alloy were removed from the substrate and measured using both pycnometry and by mass (Figure 7), with results shown as a function of the energy density. In all cases, the mass of the samples increased monotonically with energy density, while the pycnometry measured density first decreased and then increased. These results suggest that at very low energy density, the samples tend to contain a large fraction of interconnected pores, which are not measured by the pycnometer. The minimum density value occurs when the large pores begin to close off and are no longer surface-connected. The density then increased along with the mass for higher energy density parameter sets.

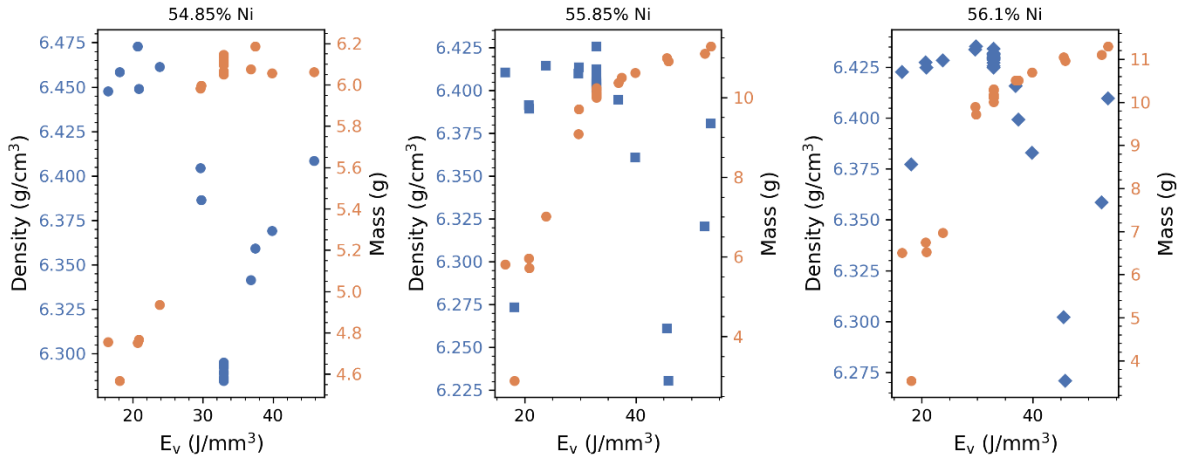

Figure 7: Pycnometer density and mass data for each of the three alloys as a function of the volumetric energy density.

The phase content of the as-fabricated samples was characterized using x-ray diffraction (XRD) for the central parameter set in each alloy. For Alloy A, the diffraction spectra for the atomized powder and as-fabricated AM sample are compared in Figure 8a. In both cases, the diffraction patterns indicate a combination of the austenite (B2) and martensite (B19') structures. However, the powder and AM samples exhibit different fractions of these phases, with Rietveld analysis showing that the powder consists of 74 vol% of the B19' structure, while this value increases to 88 vol% in the AM sample. In addition, Ni_3Ti was only observed in the AM samples and not in the powder. The precipitation of Ni_3Ti was likely suppressed during the fast cooling of the atomization process. Although the cooling rates in AM are also very high, it is possible the precipitation may occur during the multiple reheating cycles upon melting of subsequent layers. Figure 8b compares the XRD spectra for the three alloys in the as-fabricated AM condition. Generally, the increasing room temperature volume fraction of the B2 structure from Alloys A to C varies as expected with increasing Ni content (phase fractions are summarized in Table 3). Although the oxygen content for these alloys was appreciable, oxide and Ti_4Ni_2Ox type phases were not clearly visible in the XRD spectra, likely due to the low volume fraction of these structures.

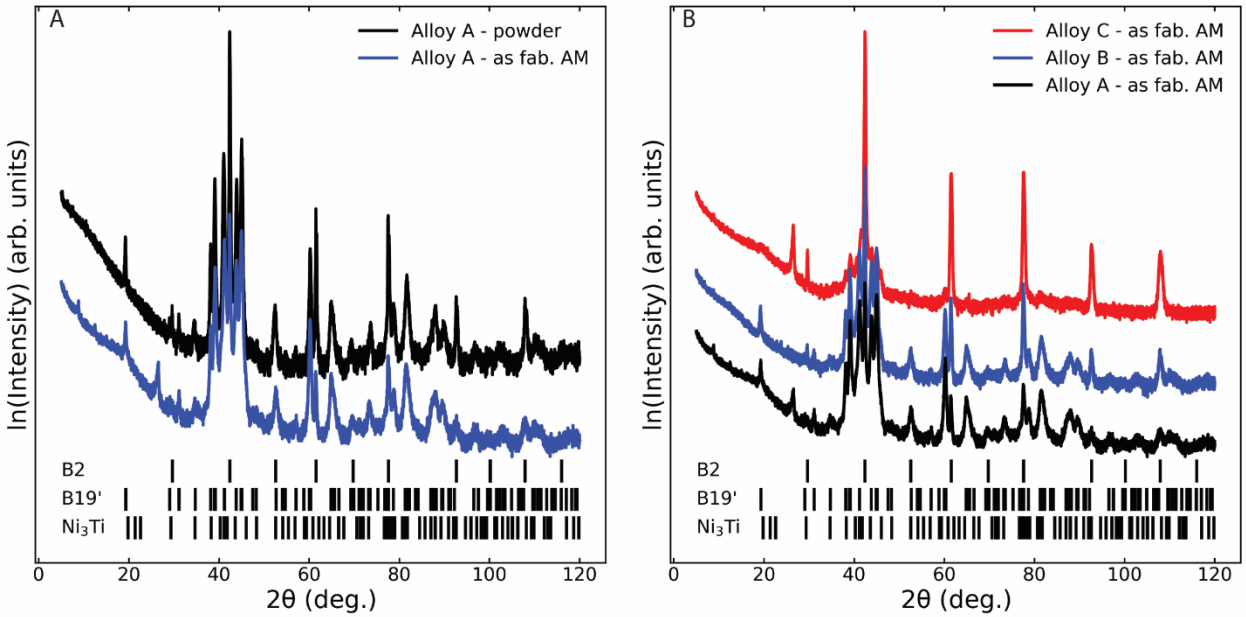

Figure 8: XRD patterns showing (a) a comparison of the powder and as-fabricated AM conditions for Alloy A, and (b) a comparison of the three alloys in the as-fabricated AM condition.

Table 3: Phase fraction determine from Rietveld analysis of powder and as-fabricated AM samples, given in volume percent.

Alloy Design	B2	B19’	Ni_3Ti
Alloy A – powder	34.0	64.0	-
Alloy A – as fab. AM	17.3	82.0	0.7
Alloy B – as fab. AM	29.5	61.9	0.8
Alloy C – as fab. AM	82.8	17.2	-

1.2.1.3 Oxygen Analysis

The oxygen content of the powders used for additive manufacturing were also measured across all of the nominally sieved size distributions and compared to the starting oxygen content from the ingots, and to the final oxygen content in the additively manufactured samples (Figure 9). The size distributions are reported relative to mean particle diameter for the nominal sieve ranges. The magnitude of the oxygen content is broadly similar to previous findings in the literature [24]. As the powder size distribution increases, the oxygen content tends to decrease. This trend is consistent with the decreasing surface area per unit volume with increasing average particle diameter [21]. Alloys A and B tend to show similar oxygen content as a function of particle size range. Alloy C however shows a significantly higher oxygen content for size ranges 53-109, 109-250, and <250 µm. The increase in oxygen content for Alloy C corresponds to higher initial oxygen content of ingot used for atomization (shown by dashed lines in Figure 9), but may have also been influenced by the powder particle morphology, in which Alloy C showed the greatest number of irregular powder particle. These types of particles were among the largest observed in the 53-109 µm sieved powder and may have been effectively removed for the finest powder size distributions, explaining why all three alloys appear similar for the nominal <20 and 20-53 µm size ranges. For the larger powder, the higher surface area of these irregular particles may have allowed for an increased level of oxygen uptake.

The specific powders used for additive manufacturing are indicated by red circles in Figure 9, and the oxygen content of representative printed samples as shown by dotted lines. The powder for Alloy A contained the highest oxygen content owing to the use of a finer powder size distribution, followed by Alloy C, while Alloy B has the lowest oxygen content. The oxygen content of the material also increased during additive manufacturing due to absorption of oxygen from the atmosphere into the high-temperature liquid melt pool. This oxygen absorption process is expected to be similar for all three alloys, assuming that minor chemistry variations have a negligible impact on the thermophysical properties of the material and subsequent melt pool behavior. Here, the oxygen increase during additive manufacturing was similar in all cases, and the major differences between the final oxygen content of the AM samples was inherited from differences in the ingot impurity content, and the absorption of oxygen by the powder as a function of powder surface area per unit volume.

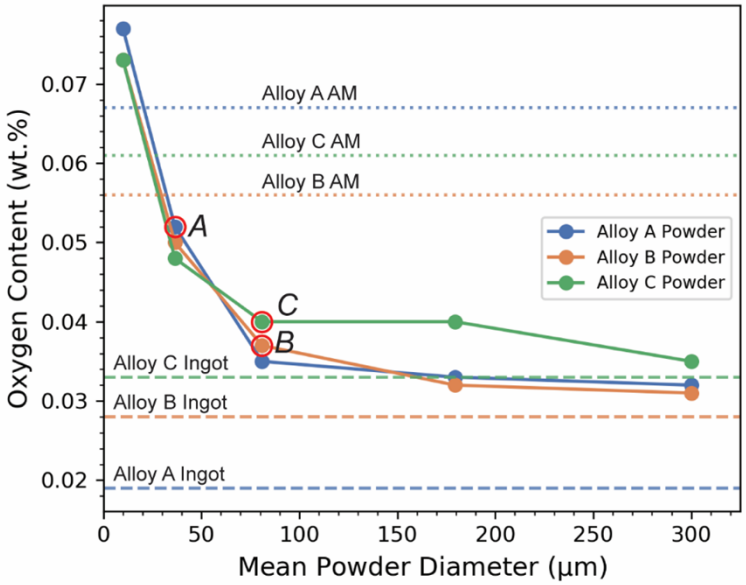

Figure 9: Oxygen content for each alloy as a function of powder size and compared to initial ingots and fabricated AM samples.

The solid-state phase transformation of the additively manufactured samples of each alloy were measured by DSC in the as-fabricated and annealed conditions and compared to the ingot and powder of the same nominal composition. The DSC curves are summarized in Figure 9. (Additional DSC data for the powder as a function of size distribution may be found in the appendix). The ingots generally show sharp single peaks, while the powder made from those ingots exhibits multiple smaller peaks. The additively manufactured material shows a smoother response than the powder, but the peaks are not as sharp as the ingots. For Alloy A, the peaks for the powder and AM material tends to occur at lower temperatures than the peaks for the ingot. However, for Alloys B and C, the peaks in the powder and AM samples are shifted to higher temperature compared to the ingot. The additional peaks observed in the powder samples may be related to solid-state precipitation, corresponding to the observed differences in Ni_3Ti phases relative to the AM material (though likely related to other secondary phases as well).

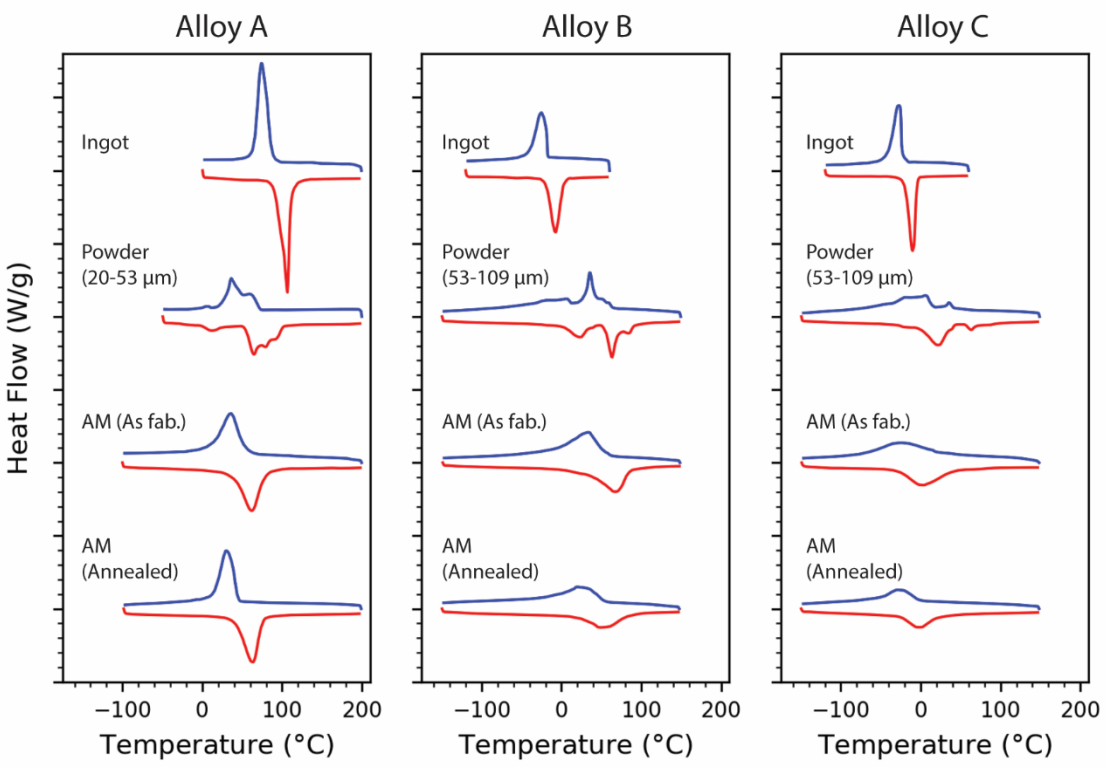

Figure 10: Comparison of DSC data for each alloy at each stage of processing.

1.2.2 Phase 2

During production of powders, a small fraction of the overall atomized powder lot is usually sieved out and used for suitability for a particular process. This process of sieving the powder for a given application significantly reduces the overall yield from the original ingot, increasing the cost and inventory of suppliers, and driving up cost for users and end products. However, different processing routes have suitability for different size ranges of powder. Therefore, the purpose of Phase 2 of this project was to evaluate the use of a single Nitinol alloy composition for different powder size distribution ranges and to perform and assess preliminary process for that composition across a range of suitable additive manufacturing processes. For this purpose, several lots of powder were first evaluated. Once a suitable batch of powder was selected, appropriate powder size ranges were selected for processing with laser powder bed fusion, directed energy deposition, and binder jet additive manufacturing processes, corresponding to nominal, over, and under-sized powder, respectively.

1.2.2.1 Alloy Selection and Powder Characterization

Based on the results from Phase 1, an alloy chemistry of nominally 50 at.% Ni with an austenitic start temperature of 90-95 °C was selected for further investigation. Powder was procured from three different powder manufacturers (denoted M1, M2, and M3) and of varying size ranges. Table 4 summarizes the received powders and the results of Hall flow testing for each with some notes on the powder flow behavior. The Hall flow results indicated that the 20-63 µm size range for manufacturer M1 was the best suited for LPBF processing, while the 50-150 µm size range from manufacturer M2 was best for DED processing. The smallest particle size and powder from manufacturer M3 did not flow.

Table 4: Hall flow measurements for powders as a function of manufacturer lot and size distribution. Powder from M1 was used for remaining studies.

SIZE	Powder Manufacturer	Hall Flow	Notes
<25µm	M1	No Flow	Does not flow, even when tapped
20-63µm	M1	17.9s	Material will flow but powder stuck to funnel. Tapping will knock it off.
50-150µm	M1	16.2s	Material will flow but powder stuck to funnel. Tapping will knock it off.
<20µm	M2	No Flow	-
20-63µm	M2	22.92s	Tap to start. Intermittent flow. Excess residual powder stuck to sides.
50-150µm	M2	16.05s	Good for DED
15-53µm	M3	No Flow	Tapping did not start flow

The quality of the powders was further analyzed by performing x-ray computed tomography (XCT) on a small samples of each using a Zeiss Versa XCT system. Figure 11 shows a summary of the XCT reconstructions for powder from manufacturer M1. The morphology of the powder particles was predominantly spherical in all cases. However, cross-sections of the reconstructed XCT data indicated some internal gas pores entrapped within a subset of the powder particles. The size distributions for each powder size range and the entrapped gas pores were quantified from the XCT results (Figure 12). The size distributions for the powder particles shows that the 20-63 µm size range actually included a large fraction of fine powder particles. The entrapped pore size in all cases was relatively small (<5µm) and accounted for a modest 0.3-0.5 vol.% of the powder.

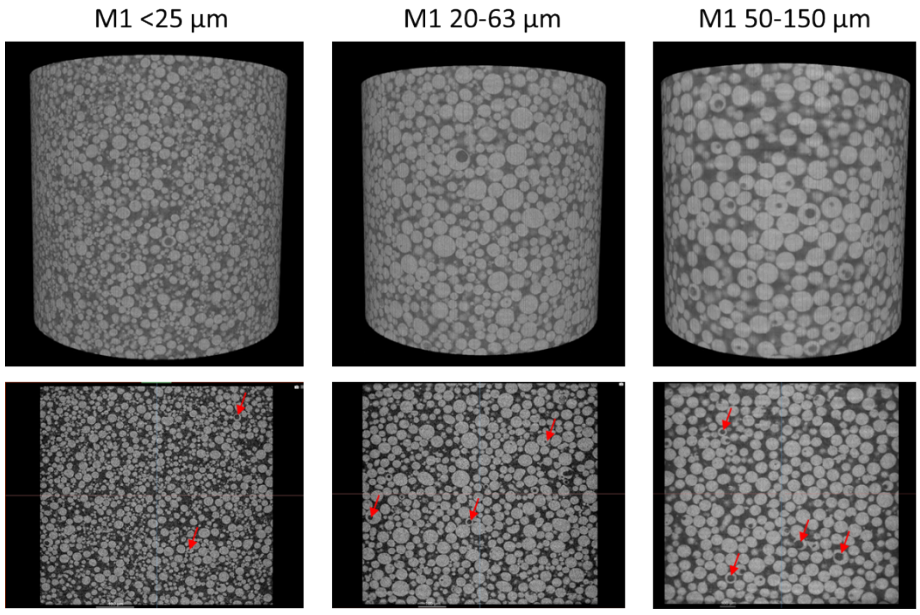

Figure 11: XCT reconstruction of powders from manufacturer M1 for different size distributions (bottom) showing cross-sections with indicated internal gas pores.

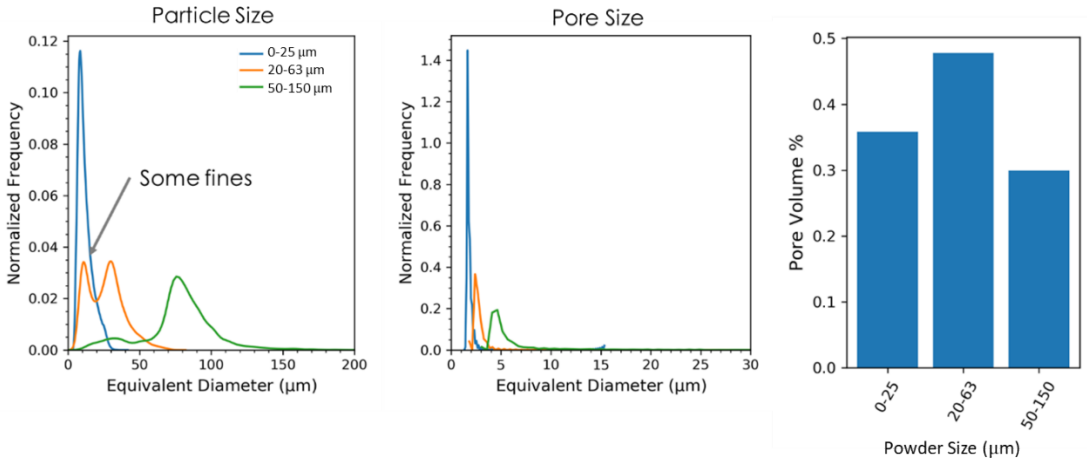

Figure 12: Powder and internal porosity size distributions, and pore volume percent for each powder size range for manufacturer M1.

A similar analysis was performed for the powder received from manufacturer M2. XCT reconstructions again showed primarily spherical particles (Figure 13). However, unlike the powders from manufacturer M1, a significant number of high-density particles were also identified as shown by the threshold reconstructed images in the bottom of Figure 13. These high-density particles are indicative of unwanted inclusions within the material.

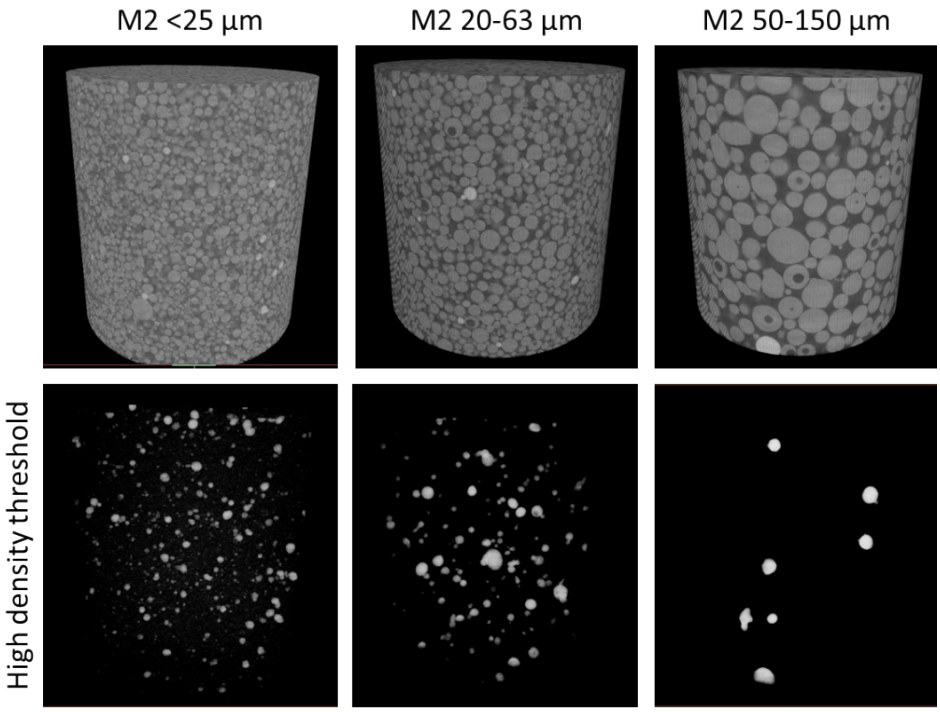

Figure 13: XCT reconstructions of powders from manufacturer M2 of varying size distributions (bottom) showing thresholds at high density indicating the presence of inclusions.

The powder particle size distributions and entrapped gas content was also analyzed for manufacturers M2 and M3 as shown in Figure 14. The 20-63 µm size range for manufacturer M2 does not show the same population of fine particles that were observed for the same particle size range from manufacturer M1. The powder from M3, despite nominally being for 15-45 µm size range, was found to primarily contain finer particles more consistent with the other 0-25 µm nominal distributions. Analysis of the entrapped gas pores showed generally lower overall fractions than those from manufacturer M1, except for the large 50-150 µm powder size range for manufacturer M2, which showed a comparatively large fraction of pores above 0.8 vol.%.

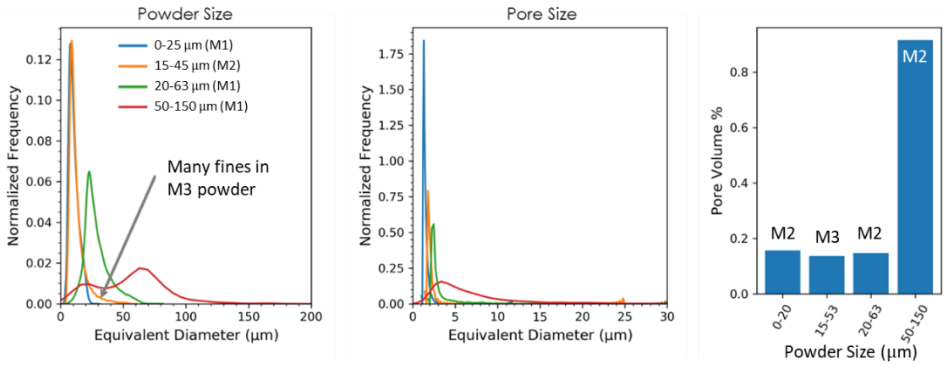

Figure 14: Powder and internal porosity size distributions, and pore volume percent for each powder size range for manufacturers M2 and M3.

In the above results, the powder size distributions for manufacturer M2 were closest to those that were expected and showed the best overall flowability behavior. However, given the sensitivity of Nitinol phase transformations to even small variations in composition, the unexpected inclusions accrued during the atomization process were deemed highly undesirable. As a result, the three powder size distributions from manufacturer M1 were selected for processing and further analysis.

1.2.2.2 Laser Powder Bed Fusion Process and Characterization

Building on the results from Phase 1, the powder from manufacturer M1 with nominal size distribution of 20-63 µm was processed using a Renishaw AM250 laser powder bed fusion AM system. First, the previous design of experiments was repeated to help identify appropriate processing parameters. The resulting build is shown in Figure 15. The parameters with the lowest level of defects (cube #10) were selected for further processing (Table 5).

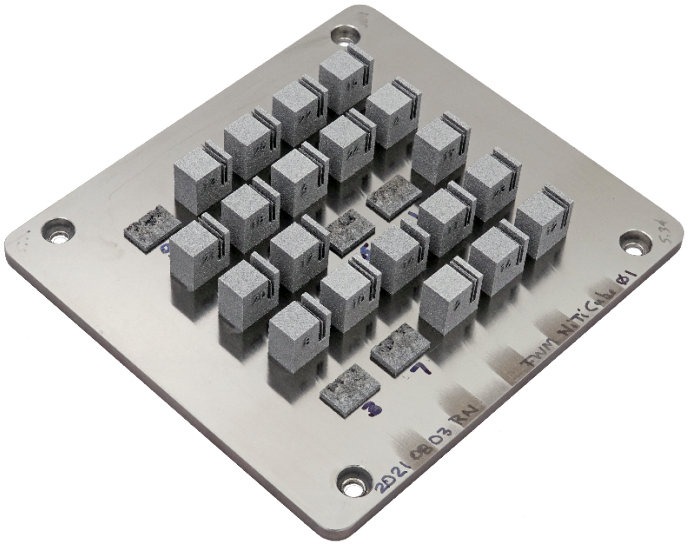

Figure 15: Photograph of the samples produced for the LPBF design of experiments.

Table 5: Selected LPBF process parameters

Parameters	Value
Layer Thickness	30 μm
Hatch	108 μm
Point Spacing	75 μm
Exp. Time	65 μs
Vol. Energy Dens.	53 J/mm^3

The selected processing parameters listed in Table 5 were used to fabricate blocks for machining into test coupons. Samples were machined from the blocks for constant force thermal cycling (CFTC). In this test, a constant force is applied while the material is thermally cycled through the transition range while the sample strain is measured. Figure 16 shows a typical test coupon an an example response curve with several important values labeled, including the hysteresis, the activation strain (e_{act}), and the residual strain (e_{res}).

The samples manufactured for testing are shown in Figure 17. Blocks were printed such that samples could be machined in three different orientations. After machining, samples were also annealed using various times and temperatures to study the effect of heat treatment on the CFTC performance. Average results of the CFTC testing for each orientation and annealing conditions are summarized in Figure 17. Orientation A, along the build direction, exhibited slightly lower activation strain than the other orientations under any set of annealing conditions. More aggressive annealing also tended to slightly decrease the residual strain for all orientations.

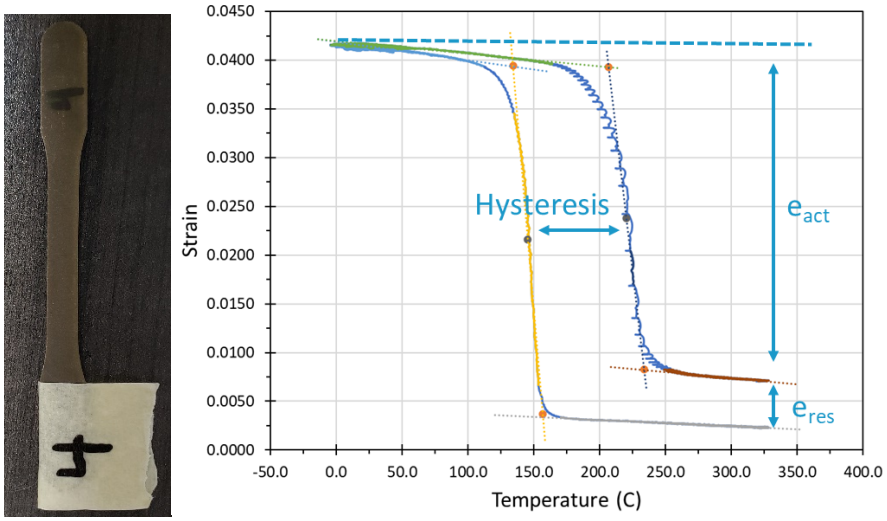

Figure 16: (Left) An example of a mechanical test coupon for constant force thermal cycling testing and (right) a schematic of an example result labeling the definitions for hysteresis, the activation strain (e_{act}) and the residual strain (e_{res}).

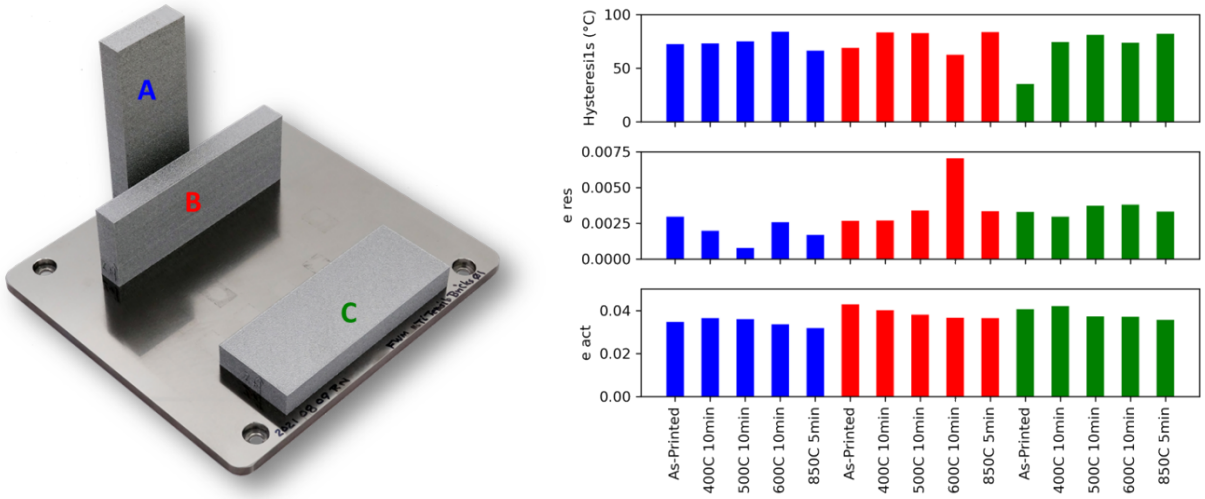

Figure 17: (Left) Photograph of LPBF build for three coupons in different orientations and (right) corresponding average results for CFTC testing.

LPBF fabricated samples were studied using temperature dependent X-ray diffraction to determine how the underlying phases evovled in response to a cyclic thermal exposure (Figure 18). Prior to heating, only peaks for the B19' phase are present. Heating above ~65°C drives the reversible transition from B19' to B2. No evidence of B19' retention is observed above 75°C. Futher heating up to 150°C does not result in any futher phase transitions. Diffraction data measure upon cooling underscore the hysteretic nature of the underlying phase transition, where B2 remains the primary phase down to 45°C. We note that samples were not cooled below the martensitic completion temperature. Exposure to a second and then third heating and cooling cycle does not affect the phase evoluiton, within experimental resolution.

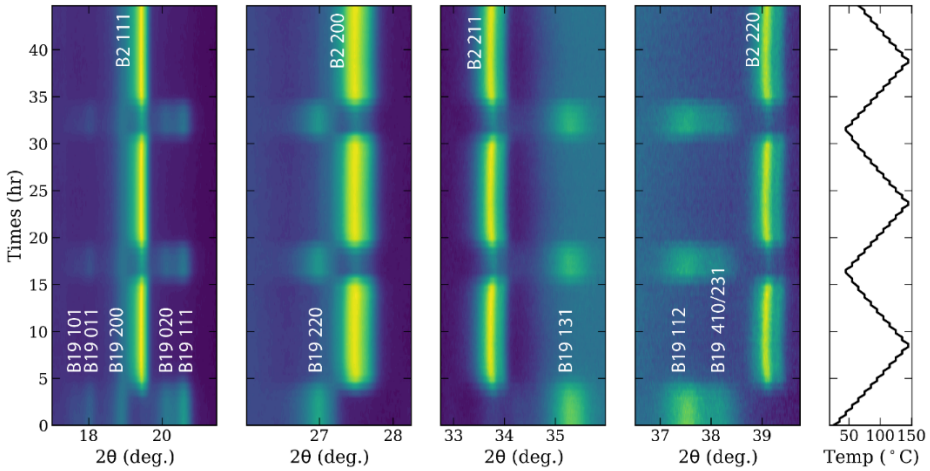

Figure 18: Time-resolved x-ray diffraction data during heat and cooling for an initially as-fabricated LPBF sample.

Representative diffraction patterns measured at 65°C during the heating and cooling portion of the thermal cycles are shown in Figure 19. Drastic differences in the B2 and B19' phase fraction at 65°C are observed for the heating and cooling segments of the thermal cycles, as evidenced by the lack of B19' peaks in the in the diffraction data measured during cooling. Peak markers for the B2 and B19' phases are shown for references. Measured diffraction data are shown from bottom to top, with the bottom most sample being measured during the initial heating cycle and the last pattern being the cooling portion of the last cycle. A slight difference in the fraction of B2 phase is observed in the 65°C heating data measured during the 1st, compared with the 2nd and 3rd heating cycles. This slight difference is attributed to the slight differences in thermal histories because the 2nd and 3rd heating cycles start from 35°C instead of RT. Data measured on cooling from 150°C are equivalent, within the resolution of the experiment.

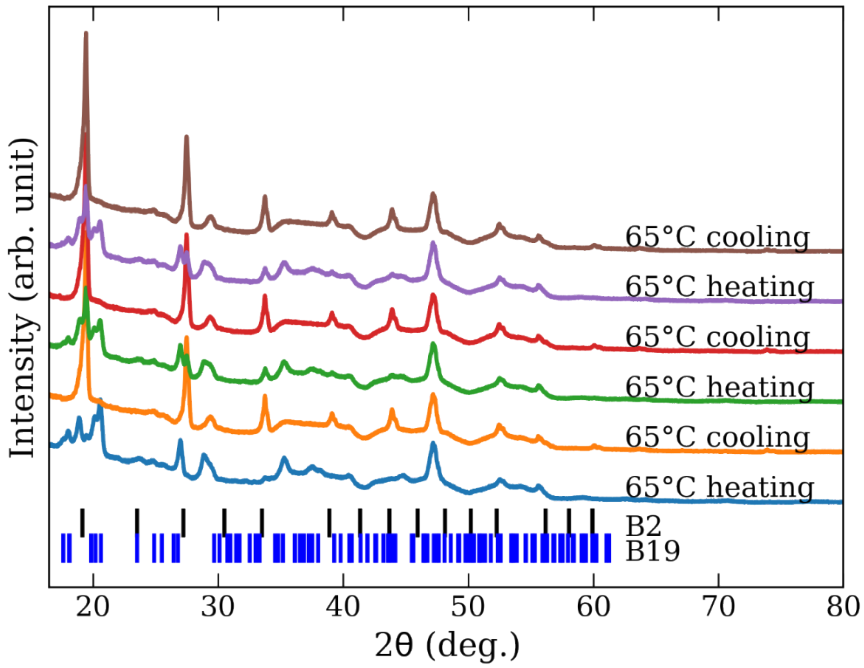

Figure 19: Representative diffraction patterns measured at 65°C for the in situ XRD experiments. Differences in the patterns measured upon heating and cooling evidence the effects of the hysteresis in the martensitic transition temperature on the observed phase fraction.

1.2.2.3 Directed Energy Deposition Processing and Characterization

Directed energy deposition process was performed using a BEAM MODULO 400 system for NiTi powder in the size range 50-150 µm. To begin with, a variety of different process conditions were evaluated to produce single bead walls and some small pads. The initial build is shown in Figure 20, and the complete list of tested processing conditions is given in Table 6. This initial study provided information for tuning the combination of laser power, scan speed, powder flow rate, and layer offset, but also produced material under a variety of processing conditions to be used to evaluate the effects of processing on the material behavior.

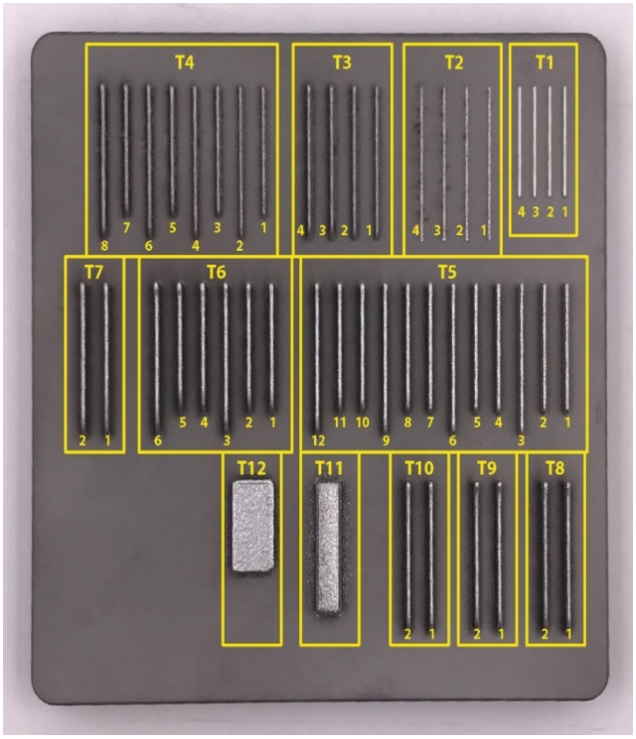

Figure 20: Photograph of preliminary DED build for thin walls.

The single-bead walls were removed from the build plate and tested in two ways. First, the oxygen content within the samples was measured to detect if the processing conditions had a significant effect on potential oxidation of the Ti content within the alloy, which can affect the shape-memory transformation behavior. Figure 21 shows a summary of the oxygen measured in each sample as a function of the laser power percentage and the programmed layer height. The overall oxygen content ranged from about 0.035 to 0.06 wt.%. It was not strongly dependent on the laser power, but tended to increase some with layer height, before decreasing for very large layer heights. The results suggest that while variation in process conditions may affect the oxygen content, the effect is not very strong, and large sample-to-sample variation was observed.

The transformation behavior of the samples were evaluated directly by differential scanning calorimetry (DSC) in both the as-fabricated and annealed conditions. Examples of these data are shown in Figure 22, as well as a summary of the distribution of austenite start temperatures. The as-fabricated samples tended to show poorly defined peaks with some indication of secondary peaks. Alternatively, the

annealed samples showed well defined peaks as expected of conventional NiTi alloys. The distributions of the austenite start temperature shows that processing parameters do have a strong effect on the as-fabricated transformation behavior. However, this effect largely diminished after annealed, producing a much narrow range of transformation temperatures across all samples. In contrast to the LPBF as-printed samples, which showed distinctive peaks but had A_s values ~20°C colder than in the heat treated condition. The DED as-printed samples had A_s values closer to the heat treated condition but did not have distinct peaks until after the heat treat.

Table 6: Processing parameters used for initial DED testing.

Test	No.	Laser (%)	Laser (W)	Velocity (mm/min)	Powder Flow Rate (g/min)	Programmed Layer Height (mm)	Raster Stepover (mm)	Perimeter (Y/N)	Perimeter Offset (mm)	Layer Count
T1	1	18	~260	2000	0	NA	NA	NA	NA	1
	2	20	~300	2000	0	NA	NA	NA	NA	1
	3	22	~345	2000	0	NA	NA	NA	NA	1
	4	24	~380	2000	0	NA	NA	NA	NA	1
T2	1	18	~260	2000	4.14	NA	NA	NA	NA	1
	2	20	~300	2000	4.14	NA	NA	NA	NA	1
	3	22	~345	2000	4.14	NA	NA	NA	NA	1
	4	24	~380	2000	4.14	NA	NA	NA	NA	1
T3	1	18	~260	2000	4.14	0.3	NA	NA	NA	20
	2	20	~300	2000	4.14	0.3	NA	NA	NA	20
	3	22	~345	2000	4.14	0.3	NA	NA	NA	20
	4	24	~380	2000	4.14	0.3	NA	NA	NA	20
T4	1	18	~260	2000	4.14	0.15	NA	NA	NA	20
	2	18	~260	2000	4.14	0.2	NA	NA	NA	20
	3	20	~300	2000	4.14	0.15	NA	NA	NA	20
	4	20	~300	2000	4.14	0.2	NA	NA	NA	20
	5	22	~345	2000	4.14	0.15	NA	NA	NA	20
	6	22	~345	2000	4.14	0.2	NA	NA	NA	20
	7	24	~380	2000	4.14	0.15	NA	NA	NA	20
	8	24	~380	2000	4.14	0.2	NA	NA	NA	20
T5	1	18	~260	2000	4.14	0.1	NA	NA	NA	20
	2	18	~260	2000	4.14	0.13	NA	NA	NA	20
	3	18	~260	2000	4.14	0.15	NA	NA	NA	20
	4	20	~300	2000	4.14	0.1	NA	NA	NA	20
	5	20	~300	2000	4.14	0.13	NA	NA	NA	20
	6	20	~300	2000	4.14	0.15	NA	NA	NA	20
	7	22	~345	2000	4.14	0.1	NA	NA	NA	20
	8	22	~345	2000	4.14	0.13	NA	NA	NA	20
	9	22	~345	2000	4.14	0.15	NA	NA	NA	20
	10	24	~380	2000	4.14	0.1	NA	NA	NA	20
	11	24	~380	2000	4.14	0.13	NA	NA	NA	20
	12	24	~380	2000	4.14	0.15	NA	NA	NA	20
T6	1	25	~405	2000	4.14	0.1	NA	NA	NA	20
	2	25	~405	2000	4.14	0.13	NA	NA	NA	20
	3	25	~405	2000	4.14	0.15	NA	NA	NA	20
	4	27	~445	2000	4.14	0.1	NA	NA	NA	20
	5	27	~445	2000	4.14	0.13	NA	NA	NA	20
	6	27	~445	2000	4.14	0.15	NA	NA	NA	20
T7	1	24	~380	2000	4.14	0.1	NA	NA	NA	20
	2	25	~405	2000	4.14	0.1	NA	NA	NA	20
T8	1	24	~380	2500	4.14	0.1	NA	NA	NA	20
	2	25	~405	2500	4.14	0.1	NA	NA	NA	20
T9	1	24	~380	2500	5.18	0.2	NA	NA	NA	20
	2	25	~405	2500	5.18	0.2	NA	NA	NA	20
T10	1	24	~380	2500	3.07	0.1	NA	NA	NA	20
	2	25	~405	2500	3.07	0.1	NA	NA	NA	20
T11 (6x30)		25	~405	2500	3.07	0.1	0.4	N	NA	20
T12 (10x30)		25	~405	2250	3.07	0.1	0.4	Y	0	20

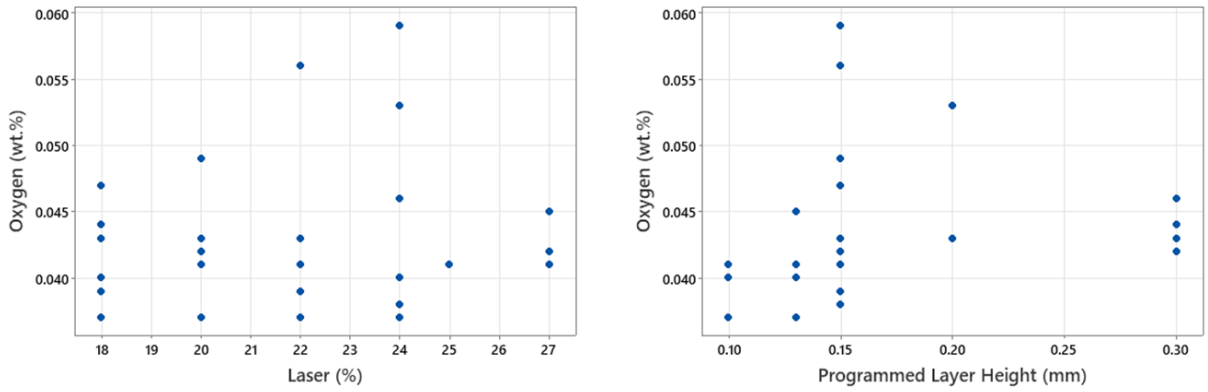

Figure 21: Oxygen content analysis for the DED printed walls, shown as a function of the laser percentage of maximum power and the programmed layer height.

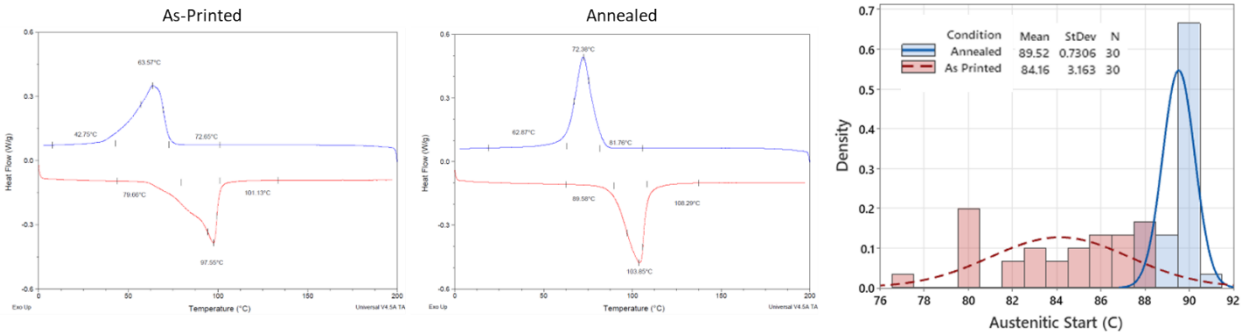

Figure 22: Example DSC data for as-printed and annealed DED samples, and (right) a histogram of the range of austenite start temperatures for the measured samples.

Based on initial testing, a design of experiments was constructed to produce multi-layer pads of the NiTi alloy. Table 7 shows the selected range of processing conditions. These parameters were used to deposit small pads of material that were then cross-sectioned and metallurgically prepared for optical microscopy in order to identify any major defects. The results of the build and microscopy analysis are shown in Figure 23. For the majority of processing conditions, cracking was observed in the deposited material (indicated by red arrows in Figure 23). However, processing conditions T17 and T18, which had a slower laser velocity and larger programmed layer height, did not have any apparent cracks. These results demonstrate that there is a range of parameters for DED that may be used to successful deposit bulk samples of this NiTi alloy without cracking.

Table 7: Processing parameters for DED study.

	Laser (%)	Laser Power (W)	Velocity (mm/min)	Powder Flow Rate (g/min)	Programmed Layer Height (mm)	Raster Stepover (mm)	Perimeter (Y/N)	Perimeter Offset (mm)
T17	25	~405	2250	3.07	0.28	0.3	Y	0
T18	25	~405	2500	3.07	0.28	0.3	Y	0
T19	25	~405	2250	3.07	0.25	0.3	Y	0.15
T20	25	~405	2500	3.07	0.25	0.3	Y	0.25
T21	25	~405	2500	3.07	0.24	0.3	Y x2	0.25
T22	22	~345	2500	3.07	0.25	0.5	Y	0.3
T23	22	~345	2500	3.07	0.15	0.5	Y	0.3

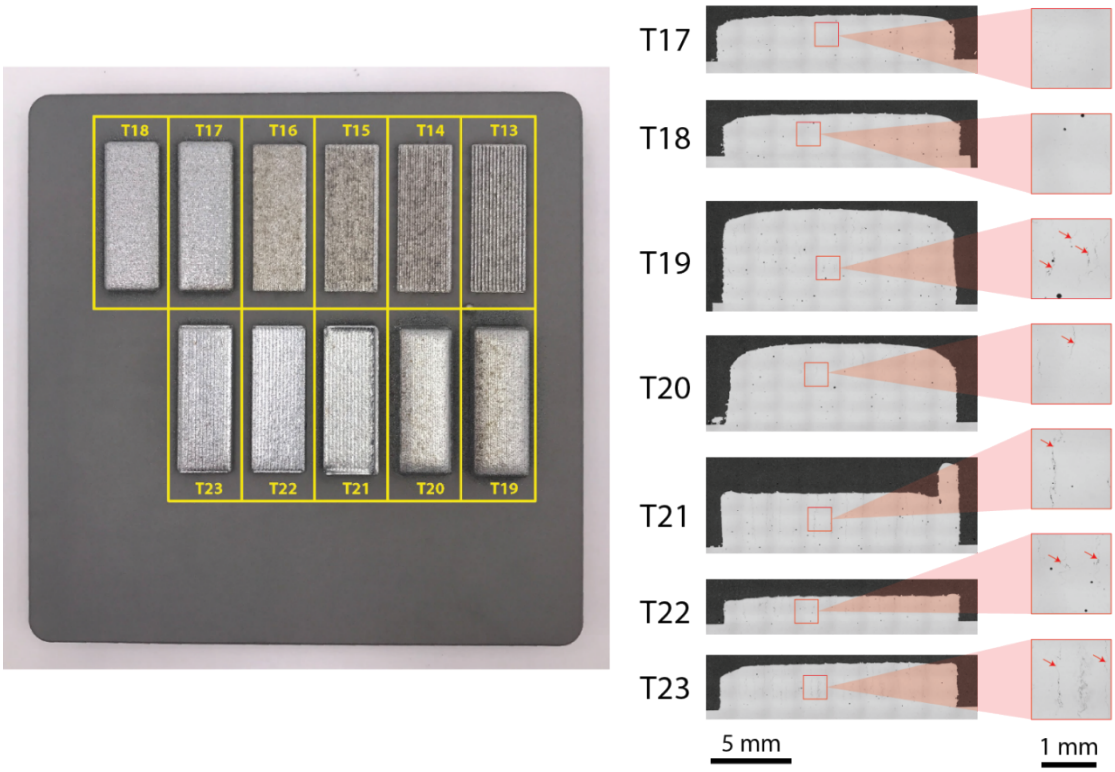

Figure 23: (Left) Photograph of completed DED build with samples labeled, and (right) stitched optical mosaics of cross sections for samples T18-T23 and higher magnification images with red arrows indicated cracks.

Based on the initial processing to identify an approximate range of acceptable processing conditions, larger deposited walls were made onto the edges of a NiTi substrate. Photographs of these deposits and associated key process variables are summarized in Figure 24. These results demonstrate that it is possible to construct bulk geometries from using the laser DED process. Additionally, the DSC data above suggests that a relatively wide range of processing parameters may be used while still obtaining shape-memory transformation behavior, provided an appropriate annealing heat treatment is applied to the finished material.

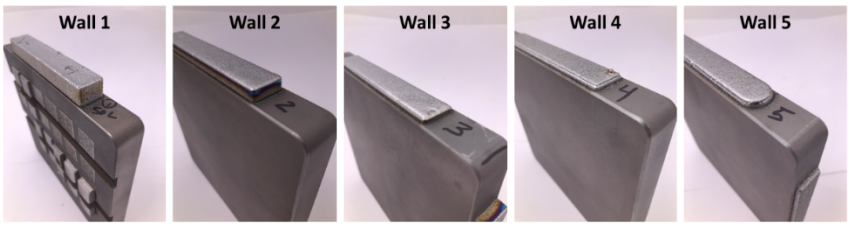

Raster vel. (mm/min)	2250	2500	2500	2500	2500
Perim. vel. (mm/min)	2000	2500	2500	2000	2000
Powder flow rate (g/min)	3.07	3.07	3.07	3.07	3.07
Layer height (mm)	0.25	0.21	0.21	0.21	0.24
Raster stepover (mm)	0.3	1.4	0.3	0.3	0.3

Figure 24: Images of powder DED walls and associated processing parameters.

1.2.2.4 Binder Jet Processing and Characterization

NiTi powder in the <25 μm size range was processed using an ExOne binder jet system. The jetting parameters were varied to produce a variety of coupons, such as examples shown in Figure 25.

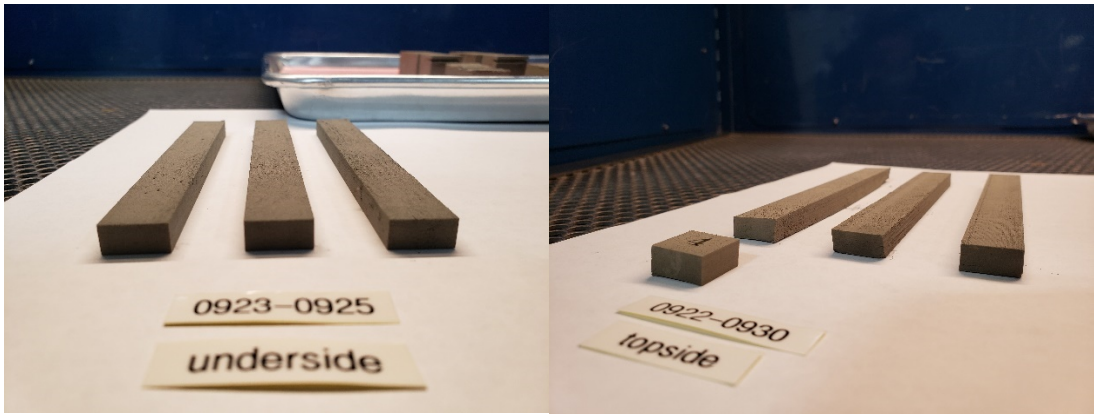

Figure 25: Photographs of example binder jet Nitinol coupons.

Several different combinations of possible sintering temperatures and times were applied to the binder jet samples. Figure 26 shows examples of three such samples. In all cases, the original geometry of the sample was highly distorted after sintering. In all cases, the samples were fragile, indicating incomplete sintering.

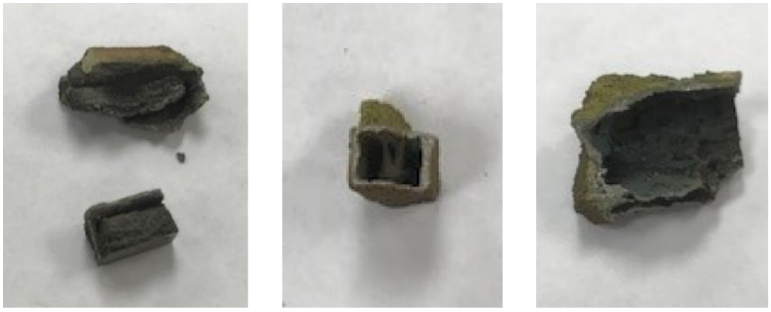

Figure 26: Examples of Nitinol binder jet coupons after sintering for various temperatures and times.

Sintered samples were also characterized using differential scanning calorimetry (DSC) to understand the effect of heat treatment time and temperature on the NiTi phase transformation behavior. These results are shown in Figure 27. In all cases, several spurious peaks in the DSC data were observed, although the corresponding breadth of these peaks and the temperatures at which they occurred was sensitive to the selected heat treatment time and temperature. Overall, these results suggest that the binder jetting and sintering process created unwanted phase transformations in the materials. These transformations could be the result of impurity content from the organic C-based binder or other elements that affected the transformation behavior of NiTi. It is possible that optimized heat treatments could improve the transformation behavior to give a more consistent and narrow shape-memory response. However, it is clearly challenging to achieve this result while maintaining the shape of the printed preform.

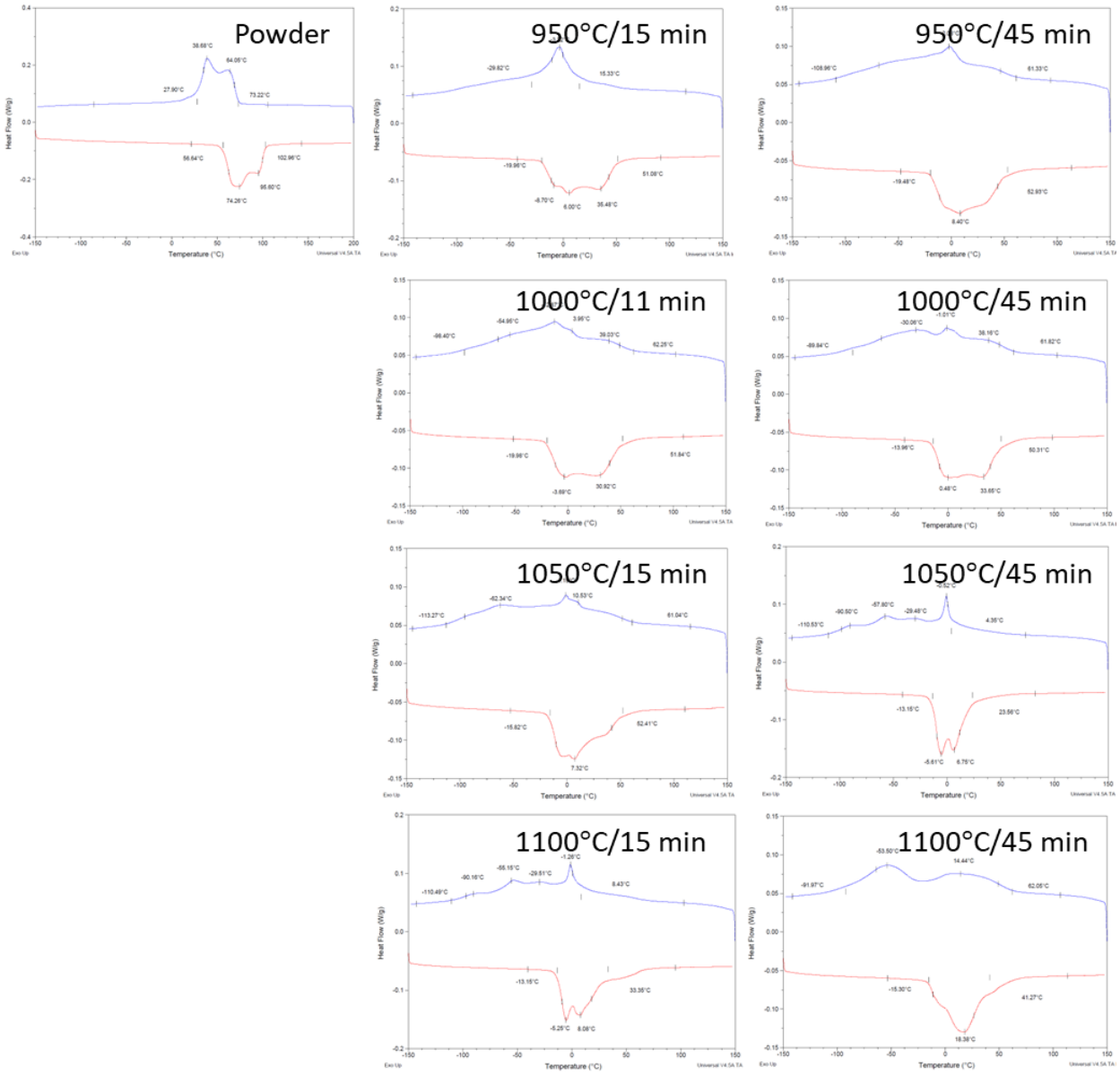

Figure 27: DSC results for NiTi powder and after annealing of binder jet coupons for various temperatures and times.

The DSC data for the binder jet samples may be explained, at least in part, by the impurity content. Oxygen will also impact the DSC values. Table 8 shows analysis of the impurity content for the as-fabricated binder jet samples. Note that the oxygen and carbon content is an order of magnitude higher than was measured in the LPBF samples. Oxidation consumes more Ti than Ni causing the transformation temperatures to decrease. Carbon does the same due to formation of TiC. The high C and O content explains why the transformation temperatures are colder after heat treatment. These results explain why the DSC analysis of the as-printed part was similar to the powder, but after the 850°C/15 minute heat treatment, the DSC curves are flat, showing little to no transformation behavior.

Table 8: Impurity content in the as-fabricated binder jet samples.

Element	Oxygen	Carbon	Nitrogen	Hydrogen
Content (wt.%)	0.501	0.412	0.129	0.054

1.4 CONCLUSIONS

In this project, we procured powder of three Nitinol alloys, spanning from shape memory to superelastic compositions, and performed laser powder bed fusion additive manufacturing. A design of experiments was performed with each of the three powder compositions to identify trends in the final component density as a function of process conditions. The solid-state phase transformation characteristics were measured via DSC, and the characteristics of the powder were also compared to the additively manufactured components. The influence of powder size on Ti depletion through oxidation was found to play a critical role in the eventual phase transformation behavior of the printed alloys. Finer powder size distributions tended to absorb more oxygen due to a higher surface area. Increased oxidation removed Ti from the alloy and reduces the transformation temperature. On the other hand, Ni vaporizes more readily during LPBF processing. Depending on the powder size, one or the other of these two effects tends to dominate the phase transformation behavior relative to conventional material, or they can balance each other. These results suggest that additional research is required to identify specifications for powder size distributions and chemistry to produce reliable phase transformation behavior in additively manufactured Nitinol components.

In the second phase of the project, a single Nitinol alloy was selected and powder of three different size distributions were evaluated for suitable processes. The smallest powder was processed using binder jet additive manufacturing, the largest using directed energy deposition, and intermediate powder with laser power bed fusion. Each process exhibited its own characteristic challenges and resulting material behavior. LPBF was the most successful for processing components with powder from its suitable size range. A significant amount of cracking was observed in the DED samples for a range of processing conditions, although smaller samples were able to be processed within a narrow processing window. The binder jet samples exhibited significant changes in sintering following initial deposition, and changes in transformation behavior consistent with increased impurity content owing to small powder size and excess carbon from the binder.

1.5 REFERENCES

[1] D.A. Porter, K.E. Easterling, Phase Transformations in Metals and Alloys, Second, Taylor & Francis Group, Boca Raton, FL, 1981.

[2] F.E. Wang, W.J. Buehler, S.J. Pickart, Crystal structure and a unique “martensitic” transition of TiNi, J. Appl. Phys. 36 (1965) 3232–3239. doi:10.1063/1.1702955.

[3] D.J. Hartl, D.C. Lagoudas, Aerospace applications of shape memory alloys, Proc. Inst. Mech. Eng. Part G J. Aerosp. Eng. 221 (2007) 535–552. doi:10.1243/09544100JAERO211.

[4] J.M. Jani, M. Leary, A. Subic, M.A. Gibson, A review of shape memory alloy research, applications and opportunities, Mater. Des. 56 (2014) 1078–1113. doi:10.1016/J.MATDES.2013.11.084.

[5] D. Stoeckel, Shape Memory Actuators for Automotive Applications Design principles, Mater. Des. 11 (1990) 302–307. doi:10.1016/B978-0-7506-1009-4.50028-7.

[6] F. Butera, Shape Memory Actuators for Automotive Applications, Adv. Mater. Process. (2008) 37–40.

[7] J. Tušek, K. Engelbrecht, R. Millán-Solsona, L. Mañosa, E. Vives, L.P. Mikkelsen, N. Pryds, The Elastocaloric Effect: A Way to Cool Efficiently, Adv. Energy Mater. 5 (2015) 1–5. doi:10.1002/aenm.201500361.

[8] M. Elahinia, N. Shayesteh Moghaddam, M. Taheri Andani, A. Amerinatanzi, B.A. Bimber, R.F. Hamilton, Fabrication of NiTi through additive manufacturing: A review, Prog. Mater. Sci. 83 (2016) 630–663. doi:10.1016/j.pmatsci.2016.08.001.

[9] C. Haberland, M. Elahinia, J.M. Walker, H. Meier, J. Frenzel, On the development of high quality NiTi shape memory and pseudoelastic parts by additive manufacturing, Smart Mater. Struct. 23 (2014). doi:10.1088/0964-1726/23/10/104002.

2. FORT WAYNE METALS BACKGROUND

Fort Wayne Metals Research Products, LLC is a leading manufacturer of precision wire-based materials that are primarily used in the world's most demanding medical applications. For more than 50 years, the company has produced an array of customized material solutions in various forms and alloy systems, along with value-added services such as prototype melting for R&D alloys, accredited testing services, and research and development support. Leveraging its Nitinol materials knowledge and ability for solving technical challenges, the company is supporting advanced manufacturing of Nitinol including additive manufacturing. Headquartered in Fort Wayne, Indiana, it has more than 1,600 employees across Indiana, Ohio, and Castlebar, Ireland.